



Publication Year	2022
Acceptance in OA	2023-01-26T14:39:01Z
Title	Vorticity and divergence at scales down to 200 km within and around the polar cyclones of Jupiter
Authors	Ingersoll, Andrew P., Ewald, Shawn P., TOSI, Federico, ADRIANI, Alberto, MURA, Alessandro, GRASSI, Davide, PLAINAKI, CHRISTINA, SINDONI, Giuseppe, Li, Cheng, Siegelman, Lia, Klein, Patrice, Young, William R.
Publisher's version (DOI)	10.1038/s41550-022-01774-0
Handle	http://hdl.handle.net/20.500.12386/33083
Journal	NATURE ASTRONOMY
Volume	6

Vorticity and divergence at scales down to 200 km within and around the polar cyclones of Jupiter

Andrew P. Ingersoll¹, Shawn P. Ewald¹, Federico Tosi², Alberto Adriani², Alessandro Mura², Davide Grassi², Christina Plainaki³, Giuseppe Sindoni³, Cheng Li⁴, Lia Siegelman⁵, Patrice Klein⁶, William R. Young⁵

¹Planetary Science, California Institute of Technology, 1200 E. California Blvd, Pasadena, CA 91125, USA

²Istituto Nazionale di AstroFisica – Istituto di Astrofisica e Planetologia Spaziali (INAF-IAPS), Rome, Italy

³Agenzia Spaziale Italiana (ASI), Via del Politecnico snc, 00133 - Rome, Italy

⁴Climate and Space Sciences and Engineering, University of Michigan, 2455 Hayward Street, Ann Arbor, MI 48109, USA

⁵Scripps Institution of Oceanography, University of California, San Diego, La Jolla, CA 92037, USA

⁶Division of Geological and Planetary Sciences, California Institute of Technology, Pasadena, CA 91125, USA. Jet Propulsion Laboratory, California Institute of Technology, Pasadena, 91109 CA. USA. LMD/IPSL, Ecole Normale Supérieure, CNRS, Paris, France

Corresponding author: Andrew P. Ingersoll, 626-376-6872, api@gps.caltech.edu

ORCIDS registered at PNAS by individual authors

Keywords: Jupiter, Juno, vortex, convection, atmosphere

This version of the article has been accepted for publication, after peer review but is not the Version of Record and does not reflect any post-acceptance improvements, or any corrections. The Version of Record is available online at <http://dx.doi.org/10.1038/s41550-022-01774-0>. Use of this Accepted Version is subject to the publisher's Accepted Manuscript terms of use <https://springernature.com/gp/open-research/policies/accepted-manuscript-terms>.

32 **Abstract**

33

34 Since 2017 the Juno spacecraft has observed a cyclone at the north pole of Jupiter surrounded by
35 eight smaller cyclones arranged in a polygonal pattern. It is not clear why this configuration is so
36 stable or how it is maintained. Here we use a time series of images obtained by the JIRAM
37 mapping spectrometer on Juno to track the winds and measure the vorticity and horizontal
38 divergence within and around the polar cyclone and two of the circumpolar ones. We find an
39 anticyclonic ring between the polar cyclone and the surrounding ones, supporting the theory that
40 such shielding is needed for the stability of the polygonal pattern. However, even at the smallest
41 spatial scale (180 km) we do not find the expected signature of convection – a spatial correlation
42 between divergence and anticyclonic vorticity – in contrast with a previous study using
43 additional assumptions about the dynamics, which shows the correlation at scales from 20 to 200
44 km. We suggest that a smaller size, relative to atmospheric thickness, of Jupiter’s convective
45 storms compared with Earth’s, can reconcile the two studies.

46

47 Plain language summary

48 The vortices at Jupiter’s poles are interesting because they are arranged in geometric patterns that
49 endure for years. The vortices are cyclones, meaning they spin counterclockwise in the northern
50 hemisphere. We confirm one theory, which says that each cyclone has to be shielded by an
51 anticyclonic ring for the pattern to be stable. We fail to confirm another study, which finds that
52 the vorticity is large where the flow is converging around an axis (the figure skater effect), and
53 vice versa. That would be evidence of convection, but we do not find it. The other study uses
54 assumptions about the dynamics to observe vorticity at scales much smaller than we do. The two
55 studies can be reconciled if convection on Jupiter is smaller relative to the atmospheric thickness
56 than convective storms on Earth.

57

58 Introduction

59

60 At Jupiter's north pole there are eight cyclones that form an octagon, with one cyclone at
61 each vertex and one additional cyclone in the center^{1,2}. The centers of the cyclones are at
62 latitudes of $83 \pm 1^\circ$, which is about 8700 km from the pole. Jupiter's south pole is the same
63 except there are only five cyclones, which form a pentagon with one at the center. The vertices
64 are at latitudes of $-83 \pm 1^\circ$. The polygons and the individual vortices that comprise them have
65 been stable for the four years since Juno discovered them^{3,4,5}. The polygonal patterns rotate
66 slowly or not at all. The peak azimuthal wind speeds around each vortex range from 70 to 100 m
67 s^{-1} , and the radial distance r from the peak to the vortex center is about 1000 km⁶. In contrast,
68 Saturn has only one vortex, a cyclone, at each pole⁷. The peak winds are 150 m s^{-1} , and the
69 radius at the peak is 1500 km^{8,9}. Saturn has a 6-lobed meandering jet at 75° , but it has no
70 cyclones associated with it. Both laboratory and theoretical models treat the hexagon as a stable
71 wave-like pattern^{10,11,12,13,14}.

72

73 There have been a handful of theoretical studies that specifically address the origin of polar
74 cyclones on Jupiter and Saturn^{15,16,17,18}. They are 1-layer and 2-layer models that introduce small-
75 scale motions either as an initial condition or as continuous forcing balanced by dissipation. The
76 small-scale vortices merge and become the large-scale vortices. The cyclones drift poleward, and
77 the anticyclones drift equatorward, as they do on Earth. In some cases the cyclones merge into
78 one big cyclone at the pole. In other cases, with different parameter settings, the cyclones wander
79 about without forming polygons. Only one theoretical study gets stable polygons from random
80 initial conditions, and only if the wavelengths of the initial random disturbances are less than 300
81 km¹⁹. A Fourier analysis of Juno data reveals that flows with wavelengths larger than 215 km are
82 gaining energy from smaller-scale flows - an example of an upscale energy transfer²⁰. Therefore
83 one goal of the present paper is to measure vorticity and divergence at scales much smaller than
84 the main cyclones and see how the upscale energy transfer takes place.

85

86 Another theoretical study²¹, which uses the shallow water equations, introduces cyclones
87 that have the observed gross properties - maximum velocity and radius, and arranges them into
88 different polygonal patterns around the pole to see which ones are stable. The stable ones have
89 shielding - a ring of anticyclonic vorticity surrounding each of the cyclones, and the unstable
90 ones do not. Some models with small-scale forcing develop shielding, but they do not organize
91 into polygons^{15,16,17,18,22}. So another goal of the present paper is to measure the vorticity inside
92 and outside the large cyclones and see whether they are shielded.

93

94 The small-scale forcing in the 1-layer and 2-layer models is a crude representation of
95 convection. There are 3D models that treat convection explicitly, in some cases with the
96 Boussinesq (quasi-incompressible) approximation^{23,24,25} and in other cases with density varying
97 vertically by up to 5 scale height^{25,26,27,28}. Some treat fluid in a box with periodic boundary
98 conditions, and others use full spherical geometry. All the 3D models have small-scale
99 convective plumes. The convective plumes produce large-scale vortices by mergers - an upscale
100 transfer of kinetic energy, and some of the vortices arrange themselves into polygonal
101 patterns^{23,28}. Although a relation between divergence and vorticity is not discussed in any of
102 these models, a negative correlation is expected for convection on a rotating planet. Therefore a

103 third goal of the present paper is to measure divergence and vorticity at scales down to 180 km
104 and look for this signature of convection.

105
106

107 Results

108
109
110

1. Scale analysis

111 At midlatitudes an important parameter is the length $L_\beta = (U/\beta)^{1/2}$ where U is a
112 characteristic horizontal velocity and $\beta = df/dy = 2\Omega\sin\theta/a$ is the latitudinal gradient of the
113 planetary vorticity $f = 2\Omega\cos\theta$. Here θ is colatitude, y is the northward coordinate, and a and Ω
114 are the planet's radius and angular velocity, respectively. L_β plays a role in the stability of the
115 zonal jets. On both Jupiter and on Saturn, $2\pi/L_\beta$ is approximately equal to the wavenumber of
116 the zonal jet profile with respect to latitude when U is the rms speed^{29,30,31,32,33}. However, L_β is
117 infinite at the poles since β goes linearly to zero there. Therefore, we introduce a different
118 scaling¹⁹, one based on minus the gradient of β at the pole, $\gamma = -d\beta/dy = 2\Omega/a^2$. The associated
119 length scale is $L_\gamma = (U/\gamma)^{1/3}$, and for $U = 80 \text{ m s}^{-1}$ it is about 10,500 km. (We ignore the
120 oblateness and use Jupiter's equatorial radius throughout this paper.) L_γ represents the radius of
121 the circle around the pole inside of which the effect of the vortices - large-scale turbulence - is
122 greater than the effect of β and the zonal jets. Note that L_γ is the distance from a specific point -
123 the pole, and L_β is not. The value of L_γ is close to the 8700 km size of the polygons on Jupiter.
124

125 The radius of deformation L_d is c/f , where c is the gravity wave speed of the gravest
126 vertical mode - the one spanning Jupiter's weather layer, which extends from the base of the
127 stratosphere down to the base of the water cloud. The value of c depends on the degree of
128 stratification of the weather layer³⁴, and is assumed to be independent of latitude. Different
129 assumptions about the vertical stratification put the average L_d at the poles in the range 350 -
130 1300 km^{34,35,36}. This brackets the 1000-km radius of the cyclones.
131

132 Originally L_β was defined as the length scale where the flow transitions from turbulence
133 to zonal jets as the scale of the flow increases³⁷. Observations of Jupiter suggest that a similar
134 transition occurs as the latitude of the flow decreases. The critical latitude, below which zonal
135 jets dominate, was shown to be a decreasing function of L_d ^{38,39}. Here we are arguing that a
136 critical latitude, $\pi/2 - L_\gamma/a$, exists even for arbitrarily small values of L_d .

137 We discuss the observations using parameters of the shallow water (SW) equations,
138 where a single layer of fluid of thickness h floats hydrostatically on a much thicker fluid, which
139 we assume is at rest^{40,41}. The two dependent variables are the horizontal velocity \mathbf{v} and the
140 gravitational potential $\phi = g_r h$, where g_r is the reduced gravity -- the gravitational acceleration
141 times the fractional density difference $\Delta\rho/\rho$ between the two layers⁴¹. ϕ is the column density in
142 the 2D continuity equation, and $\sqrt{\phi}$ is the gravity wave speed c . Also, ϕ enters in the potential
143 vorticity (PV), which is a dynamical scalar that is conserved on fluid elements. For the SW
144 equations PV is $(\zeta + f)/\phi$, where $\zeta = (\nabla \times \mathbf{v}) \cdot \hat{\mathbf{k}}$ is the relative vorticity -- the curl of the
145 horizontal velocity. 3D effects are not completely ignored - they enter through L_d , which is

146 proportional to the square root of the layer thickness h and the fractional density difference
 147 $\Delta\rho/\rho$. Even these quantities are uncertain, so given the paucity of information about vertical
 148 structure, it is best to discuss our observations with the SW equations.

149
 150

151 2. Vorticity and divergence

152 Fig. 1 shows the octagon of cyclones surrounding the north pole². Features in the clouds
 153 are visible at scales down to ~ 100 km, which is much less than the 1000-km radius where the
 154 azimuthal velocity is greatest. The figure was made from infrared images taken by the Jupiter
 155 Infrared Auroral Mapper (JIRAM) on February 2, 2017. The JIRAM M filter tracks the clouds at
 156 $4.5\text{-}5.0\ \mu\text{m}$ wavelength⁴². The image numbers used in this analysis are listed in Supplementary
 157 Table S1 of the Supplementary Information (SI). The geometrically-located images, projected
 158 onto the tangent plane at the pole, are Source Data Table SD1. The derived velocity vectors are
 159 Source Data Table SD2.

160

161 Fig. 2 shows vorticity and divergence maps for two independent determinations of the
 162 wind field. The measurement requires tracking clouds in a pair of JIRAM images separated in
 163 time to get velocity, and then taking closed line integrals to get vorticity and divergence. The
 164 magnitude of the vorticity is larger than that of the divergence. The persistence and movement of
 165 vorticity features, even those ~ 180 km in size, shows that the small-scale features are not
 166 measurement noise. The motion is visible when one blinks the left and right vorticity maps in
 167 Fig. 2 back and forth, as one can do with Supplementary Figures S1-S4.

168

169 3. Planetary signal and measurement noise

170 In Fig. 3, the top two panels show covariances between n0103 and n0204, which are the
 171 two independent determinations of the wind fields in Fig. 2. Vorticity is top left, and divergence
 172 is top right. If the measurements were perfect, the two measurements would always agree, and
 173 the arrays of points would collapse to diagonal straight lines with unit slope. The vorticity
 174 measurements come close to this ideal, with a correlation coefficient η of 0.729. Since the
 175 measurement noise is uncorrelated with the variation of vorticity on the planet, the noise and
 176 planetary variances add (Equation 1a). And since the noise from n0103 is uncorrelated with that
 177 from n0204, the covariations do not contain the variance of measurement noise (Equation 1b):

$$178 \quad \overline{(x - \bar{x})^2} = \overline{(y - \bar{y})^2} = \sigma_p^2 + \sigma_n^2, \quad \overline{(x - \bar{x})(y - \bar{y})} = \sigma_p^2 \quad (1a,b)$$

$$179 \quad \frac{\overline{(x - \bar{x})(y - \bar{y})}}{\overline{(x - \bar{x})^2}^{1/2} \overline{(y - \bar{y})^2}^{1/2}} = \eta = \frac{\sigma_p^2}{\sigma_p^2 + \sigma_n^2} \quad (2)$$

180 The quantities involving x and y are measurements and are known, so the measured correlation
 181 coefficient η allows one to determine separately the variance σ_p^2 of vorticity on the planet and the
 182 variance σ_n^2 of measurement noise. The same reasoning applies to the divergence (Fig. 3, upper
 183 right).

184 Table 1 shows the results for different values of the dimensions of the box used to
 185 measure vorticity and divergence. For the upper right panel and the 180x180 box, $\eta = 0.299$,

186 meaning that there is some divergence on the planet, but its variance is less than the
 187 measurement noise. Note that the noise values for vorticity and divergence are about the same
 188 for the same box size. The difference is that divergence decreases by a factor of 4.34, and
 189 vorticity decreases only by a factor of 1.61 from the 90x90 box to the 360x360 box. This
 190 difference is an indication that the divergence is a small-scale phenomenon that averages out for
 191 the larger boxes. For the lower two panels of Fig. 3, divergence is plotted on the y-axis with
 192 vorticity on the x-axis, and the correlation coefficient is essentially zero. Supplementary Table
 193 S2 shows that the noise estimates in the fourth column of Table 1 are best fit by assuming the
 194 measurement uncertainty for each component of velocity is 7.8 m/s.

195

196 **4. Potential vorticity and shielding**

197

198 Fig. 4 shows the azimuthal mean \bar{v} of the azimuthal velocity around the central cyclone
 199 as a function of radius r out to 6000 km. Also shown are the mean relative vorticity $\bar{\zeta}$, the mean
 200 gravitational potential $\bar{\phi}$, and the mean potential vorticity $\bar{P}\bar{V}$. In each panel there are three
 201 smooth curves. The middle one, colored orange, is derived by a linear least squares fit to the
 202 velocity data. The basis functions are given in the Methods section. The profile of $\bar{v}(r)$ agrees
 203 with earlier estimates⁶, including the fact that the profile at $r > 2000$ km falls off faster than $1/r$,
 204 implying negative vorticity in that region. Note that the fitted curve fits the data even where the
 205 velocity becomes negative (clockwise) at 4000-6000 km radial distance. The tabulated data are
 206 in Source Data Table SD3.

207

208

209 The gravitational potential ϕ in Fig. 4 is computed from an integral and is therefore
 210 uncertain by an additive constant. However, $\phi = g_r h$ is proportional to the thickness, and the
 211 thickness cannot be negative. The local maximum of ϕ is at $r = 4075$ km, and the figure is
 212 computed with $\phi = 124 \times 10^3 \text{ m}^2\text{s}^2$ there. Having $\phi > 0$ at the origin requires $\phi > 69 \times 10^3 \text{ m}^2\text{s}^2$
 213 at $r = 4075$ km. This gives $L_d > \sqrt{\bar{\phi}/f} = 749$ km at $r = 4075$ km, which is in the middle of
 214 estimates obtained from lower latitudes taking the variation of f with latitude into account^{34,35,36}.
 215

216

216 **Discussion**

217

218 In a SW model that starts with cyclones of the observed size and velocity arrayed in
 219 polygonal patterns around the jovian pole, stability requires an anticyclonic ring - shielding -
 220 around each cyclone²¹. With peak azimuthal velocity of 80 m/s and radius at the peak of 1000
 221 km, a single parameter b controls the shape of the velocity profile and the depth of the shielding.
 222 The other free parameter is L_d , but it has only a small effect on the results. Mainly the polygons
 223 are stable in the range $1 < b < 2$. Below this range, the shielding is too weak and the vortices
 224 merge. Above this range, the negative vorticity is too strong, and the anticyclonic rings become
 225 two satellites orbiting around the cyclone 180° apart. At $b > 3$, these tripoles are unstable and the
 226 polygons fly apart chaotically. The blue curve in Fig. 4 has $b = 1.35$, which is safely in the stable
 227 zone according to the SW model. The green curve has $b = 1.10$, which is right on the edge.
 228 Moreover, the minimum vorticity in the ring is $-0.27 \times 10^{-4} \text{ s}^{-1}$, which compares favorably with
 229 the model value of $-0.21 \times 10^{-4} \text{ s}^{-1}$ for $b = 1.35$. The model results are for isolated cyclones; they
 230 do not capture the change in sign of velocity at $r \approx 4000$ km or the upturn of vorticity beyond
 231 5000 km, both of which reflect the presence of circumpolar cyclones circling the pole.

232
233
234
235
236
237
238
239
240
241
242
243
244
245
246
247
248
249
250
251
252
253
254
255
256
257
258
259
260
261
262
263
264
265
266
267
268
269
270
271
272
273
274
275
276

The 200-km scale of vorticity and divergence is at least consistent with convection, Severe thunderstorms on Earth have diameters of 30-40 km, which is about 5 times the pressure scale height^{44,45}. Granules, which are the convective elements in the solar photosphere, are about 1000 km in diameter⁴⁶, which is also about 5 times the scale height of the partially ionized hydrogen gas. The scale height on Jupiter is about 40 km at the water cloud base, so if the ratio of horizontal diameter to scale height were 5, as it is on Earth and the Sun, then convection elements on Jupiter would have diameters of 200 km. This is about the smallest scale we can measure.

The bottom row of Fig. 3 shows no correlation between divergence and vorticity, although both positive and negative values are present. The implications for convection are uncertain. On the one hand, if a parcel conserves PV around a cycle of updrafts and downdrafts, the material derivative of $\zeta + f$ is proportional to the material derivative of ϕ throughout the cycle. But since ϕ is proportional to the thickness h , the material derivative of ϕ is also proportional to minus the divergence $\nabla \cdot \mathbf{v}$. Equivalently, the material derivative of negative (i.e., anticyclonic) vorticity ζ is proportional to the divergence. As a result, negative vorticity lags the divergence by a quarter cycle and there is no measureable correlation. On the other hand, if a parcel has its vorticity reset to zero at the start of each updraft, then negative vorticity develops on rising trajectories, because they diverge at the top. In this case there is a correlation between divergence and negative vorticity, and that would be a sign of convection.

Our feature-tracking approach gives vorticity and divergence at spatial scales of 200 km and larger. An entirely different approach²⁰ is to use infrared brightness itself as a dynamical variable, which extends the spatial scale down to wavelengths of ~ 15 km. The study assumes that negative infrared brightness anomalies, which are related to cloud height, are upward displacements of pressure surfaces and therefore a measure of anticyclonic vorticity. The assumption is verified at scales from 250 to 1600 km, which is smaller than the large cyclones but large enough so that feature tracking is possible. It further assumes that the flow is quasigeostrophic, so the divergence is given by $-1/f$ times the material rate of change of vorticity. This is the surface quasigeostrophic (SQG) model^{47,48}, which is used in meteorology and oceanography^{49,50}. Applied to Jupiter²⁰, one observes the signature of convection - a negative correlation between divergence and vorticity at 100 km scales and an upscale energy transfer from scales less than ~ 200 km to scales greater than ~ 200 km. These scales are just below the reach of our feature tracking method. However, the quasigeostrophic approximation is based on $Ro = \zeta/f \ll 1$, where Ro is the Rossby number. The inequality is not strictly valid for Jupiter's polar cyclones (Fig. 4), and it is even less valid at smaller scales, since Ro is predicted to increase with horizontal wavenumber⁴⁷.

At midlatitudes a *downscale* energy transfer is observed⁵¹, from wavelength scales of 2000 km to the shortest scale measured, which is about 500 km. That study uses Cassini visible light imaging; ours uses Juno infrared imaging; and SQG uses infrared brightness. More work is needed to reconcile these three data sets. A parallel study⁵² of Jupiter's south polar vortices, focusing on vorticity and stability, is a step in the right direction.

277

278 **Methods**

279

280 A series of 12 images was started every 8 minutes to cover the same region at the north
281 pole of Jupiter. Ideally the images in a series would fit together like tiles in a mosaic with no
282 overlap and no spaces in between. The spacecraft was approaching Jupiter, and the image
283 resolution changed from 22 km/pixel in the middle of the first series to 14 km/pixel in the middle
284 of the fourth series, 24 minutes later. The two maps on the left of Fig. 2 were made by measuring
285 cloud displacements between the first and third series, which are 16 minutes apart, and the two
286 maps on the right were made from the second and fourth series, which are also 16 minutes apart.
287 Therefore, the left and right maps are separated in time by only 8 minutes, but they use entirely
288 different images.

289 Supplementary Table S1 in the Supplementary Information (SI) gives the archival
290 filenames and our working names for the 48 images that were used in the analysis. The four
291 series are named n01 to n04, each of which records roughly the same place on the planet 8
292 minutes after the one before. The first step in the processing is to determine the precise location
293 on the planet of each resolution element in each image. This is done with NAIF/SPICE data from
294 the spacecraft and precise geometric calibration of the JIRAM instrument. The second step is to
295 map the brightness patterns onto a grided reference plane tangent to the planet at the pole. We
296 used 15 km/pixel for this mapping. That data is Source Data Table SD1.

297 The third step is to measure cloud displacements in the reference plane using the
298 Tracker3 software from JPL. The software automatically searches for the best correlation of
299 brightness patterns between two images. This is done between images in series n01 and n03 and
300 between images in series n02 and n04. Velocity is the displacement in km divided by the time
301 interval, which is always close to 16 minutes but depends on which image in each series was
302 used. Correlation is done within a square box in the reference plane. After experimenting we
303 settled on a 15 x 15 pixel correlation box for the Tracker3 software. Thus, with 15 km/pixel in
304 the reference plane, we are using squares 225 km on a side to define a feature. Therefore, the
305 resolution of the wind measurement is ± 112.5 km. We oversample it by a factor of 2.5 to obtain
306 wind vectors on a 45 x 45 km grid. That data set is Source Data Table SD2. We determine
307 vorticity and divergence at every grid point by integrating around boxes of various sizes using
308 Stokes's theorem and Gauss's law, respectively. Table 1 gives results for boxes 2, 4, 6, and 8
309 pixels on a side, corresponding to 90, 180, 270 and 360 km on a side, respectively.

310 The error in the velocity estimate σ_v depends crucially on the granularity of the scene at
311 the scale of the resolution element δ , which on average is about 18 km. Except for no features at
312 all, for which there is no estimate, the worst case is a single cloud feature of size $\leq \delta$, for which
313 the variance $\sigma_v^2 = 2\delta^2/\Delta t^2$, where Δt is the 16-minute time step and the factor of 2 arises because
314 we are subtracting position in two images. Then $\sigma_v = 2^{1/2}\delta/\Delta t$, about 26.5 m/s. However, if the
315 velocity measurement is the average of N statistically independent estimates of velocity, the
316 variance is $2\delta^2/\Delta t^2/N$. The best case is when N is the number of resolution elements in the
317 correlation box, which is L on a side such that $N = (L/\delta)^2$. Then $\sigma_v = 2^{1/2}\delta/\Delta t/N^{1/2} = 2^{1/2}\delta^2/L/\Delta t$,
318 which is 2.1 m/s for $L = 225$ km. Thus σ_v is highly uncertain, but in Supplementary Table S2 we
319 show that $\sigma_v = 7.81$ m/s gives a good fit to the noise column in Table 1.

320 A quantitative measure of granularity is image entropy H^{43} . We define it for each 15 x 15
 321 correlation box from the histogram of brightness values in the box:

$$322 \quad H = -\sum p_k \log_2(p_k) \quad (1)$$

323 The input data are 32-bit numbers, but we only have 225 pixels. We divide the range from the
 324 brightest to the darkest pixel into 256 grey levels, and we count the number of times that each
 325 grey level appears in the image. That number divided by 225 is p_k , the frequency of occurrence
 326 of grey level k normalized so that $\sum p_k = 1$. The sum is over the 256 grey levels. If the
 327 brightness corresponding to a particular grey level k_1 does not occur in the image, then $p_{k_1} = 0$.
 328 At least 31 of the p_k 's must be zero. If all 225 pixels have brightness corresponding to grey level
 329 k_2 , then $p_{k_2} = 1$ and all the other p_k 's = 0, resulting in $H = 0$. If the brightness levels of all the 225
 330 pixels are different, then $H = \log_2(225) = 7.81$. This is the maximum entropy for this problem.
 331 Low entropy is bad for feature tracking, and we experimented to find a value that eliminated the
 332 most suspicious data, like the large pixel-to-pixel variations in the upper left and lower right
 333 corners of the divergence maps. We manually verified that the feature-tracking software was
 334 failing in those regions. Supplementary Figure S5 is a histogram of entropy values, and
 335 Supplementary Figures S6 and S7 compare the vorticity and divergence maps with the low
 336 entropy data present and with them masked out.

337 The data of Fig. 4 consist of $\sim 26,000$ measured velocity vectors on the 45 x 45 km grid
 338 whose radius from the vortex center $r < 6010$ km. Taking the azimuthal component $\bar{v}(r)$ of each
 339 vector, and knowing its r , we did two separate least squares fits, one for the a_n and the other for
 340 the b_n in Equation (2) to get analytic expressions for $\bar{v}(r)$ and $\partial\bar{\phi}(r)/\partial r$, respectively.

$$341 \quad \bar{v} = \sum_1^4 a_n r^n + \frac{a_5 r}{(r^2 + r_0^2)}, \quad \frac{\partial\bar{\phi}}{\partial r} = -\frac{\bar{v}^2}{r} - 2\Omega\bar{v} = \sum_1^4 b_n r^n + \frac{b_5 r}{(r^2 + r_0^2)}. \quad (2)$$

342
 343 This choice of functions has no physical significance. The functions were chosen simply to fit
 344 the data and provide analytic expressions for integration and differentiation. For a good fit, the
 345 parameter r_0 must be close to the radius of the velocity maximum. Based on visual inspection, it
 346 was chosen to be 1060 km for $\partial\bar{\phi}/\partial r$ and 1200 km for \bar{v} . We analytically integrated the
 347 expression for cyclostrophic balance in Equation (2) to get $\bar{\phi}(r)$ in Fig. 4, and we analytically
 348 differentiated the expression $(1/r) \partial(r\bar{v})/\partial r = \bar{\zeta}$ to get vorticity. The table of measured
 349 azimuthal velocities is Source Data Table SD3.

350
 351

352 Acknowledgments

353

354 This research was carried out at the California Institute of Technology under a contract
 355 with the National Aeronautics and Space Administration (NASA), Grant/Cooperative Agreement
 356 Number 80NSSC20K0555, which was awarded to API, and a contract with the Juno mission,
 357 which is administered for NASA by the Southwest Research Institute. CL was supported by the
 358 51 peg-b Postdoctoral Fellowship. JIRAM was supported by the Italian Space Agency through
 359 ASI-INAF agreements n. I/010/10/0, 2014-050-R.0, 2016-23-H.0 and 2016-1495 f23-H.1-2018.
 360 AA, AM, DG, and FT were supported by INAF. CP and GS were supported by ASI. LS is

361 funded by the Scripps Institution of Oceanography Postdoctoral Fellowship. PK acknowledges
362 funding from JPL/NASA.

363

364

365 **Author Contributions:** API led the research and wrote the document. SPE did the data analysis
366 and prepared the figures. FT prepared the geometric tables that were used in the analysis. AA,
367 AM, DG, CP, and GS oversaw the successful functioning of the JIRAM instrument and provided
368 expertise on using it for image processing. CL, LS, PK and WRY provided expertise on vortices.

369

370 **Competing Interest Statement:** No competing interests

371

Box size km x km	Correlation	Signal	Noise
vort 90 x 90	0.501929	0.754479	0.751573
vort 180 x 180	0.728803	0.623902	0.380587
vort 270 x 270	0.861097	0.556075	0.223338
vort 360 x 360	0.816752	0.469033	0.222166
div 90 x 90	0.243513	0.435793	0.768104
div 180 x 180	0.299018	0.264942	0.405655
div 270 x 270	0.277184	0.1736	0.223076
div 360x360	0.289037	0.100508	0.157633

372

373 **Table 1. Standard deviations of vorticity and divergence for four different sizes of the box**
374 **used to measure vorticity and divergence. Both signal and noise have units of 10^{-4} s^{-1} . The**
375 **correlation coefficient η is dimensionless.**

376

377

378

379

380

381
382
383
384
385
386
387
388
389
390
391
392
393
394
395
396
397
398
399
400
401
402
403
404
405
406
407
408
409
410
411
412
413
414
415
416
417
418

Figure Legends

Fig. 1. Infrared image of the northern hemisphere as seen by JIRAM². The circle at 80° latitude is about 12,000 km from the pole. The lines of constant longitude are 15° apart. The radiances have been corrected for nadir viewing, with bright yellow signifying greater radiance and dark red signifying lesser radiance. The average brightness temperature is in the range 215-220 K. The figures shown in Fig. 2 of this paper cover the central cyclone and the two cyclones at 135° and 315° east longitude, respectively. The two dark features at 120-150° east, 86° north, whose filaments spiral toward their centers in a clockwise direction, are anticyclones.

Fig. 2. Vorticity (top row) and divergence (bottom row) derived from two independent determinations of the wind - left and right - termed n0103 and n0204. Each determination is derived from two sets of 12 adjacent images. The sets are ordered in time. n0103 is derived from the first and third sets, which are 16 minutes apart and overlap in time with the second and fourth sets, which are also 16 minutes apart. Thus, the interval between n0103 and n0204 is 8 minutes. The gaps between the 12 images are visible as faint vertical lines, which are especially prominent in n0204. The amorphous white spaces are regions – masks - where the image entropy⁴³ was below a threshold needed for reliable cloud-tracked wind analysis. They cover 1.8% and 2.1% of the pixels in the left and right determinations, respectively. The entropy histogram, with the dividing line below which the masks were applied, and the images with and without masks, are given in Supplementary Figures S5, S6 and S7. The long dimension of the four large rectangles in Fig. 2 is ~20,000 km, and the smallest resolved features are ~100 km in diameter. The central cyclone and the two cyclones at lower left and upper right almost disappear in the divergence maps, but the cyclones at upper left and lower right do not, mainly because the image entropy is low and the velocity error is high. The latter two cyclones are at 90° and 270°E in Fig. 1. The resolution of the original images ranges from 22 to 14 km/pixel. The resolution of the derived velocity field is 45 km. We use Gauss' Law and Stokes' Theorem to calculate divergence and vorticity, integrating around a square box that is 180 km on a side. The color bars are in units of 10⁻⁴ s⁻¹. The step sizes for the colors are 0.25 and 0.15 x 10⁻⁴ s⁻¹ for vorticity and divergence, respectively.

419 Fig. 3. Covariances of the vorticity and divergence fields of Fig. 2. Each point on the graph
420 comes from a unique point on the planet. Units along the axes are 10^{-4} s^{-1} . In the upper left and
421 upper right panels the points are plotted according to their values from two independent
422 determinations of the wind field, n0204 on the y-axis and n0103 on the x-axis. Vorticity is in the
423 upper left panel and divergence is in the upper right. As explained in the caption to Fig. 2, the
424 time interval between the two determinations is 8 minutes. At 80 m/s, which is about the
425 maximum speed of the clouds, a feature moves 38 km. This is considerably less than the 180 km
426 box size used to measure vorticity and divergence. Thus to a good approximation the two
427 determinations show the same cloud features at the same time. The small motion is still visible,
428 however, when it takes place on a large scale and includes many small-scale, high-contrast
429 features, as with the slight rotation of the features visible in Fig. 2 and Supplementary Figures
430 S1-S4.

431

432 Fig. 4. Mean azimuthal velocity and vorticity (top row) and mean gravitational potential and
433 potential vorticity (bottom row). The fitted curve for velocity (orange) is almost covered by the
434 data points (black). The peak relative vorticity ζ at the pole is $2.9 \times 10^{-4} \text{ s}^{-1}$, and is almost equal to
435 the polar planetary vorticity f , which is $3.5 \times 10^{-4} \text{ s}^{-1}$. Potential vorticity is scaled by 2.843×10^{-9}
436 $\text{m}^{-2} \text{ s}$, which is f at the pole divided by ϕ assuming it is equal to $L_d^2 f^2 = 124 \times 10^3 \text{ m}^2 \text{ s}^2$,
437 corresponding to $L_d = 1000 \text{ km}$. With this assumption, the scaled PV at the pole is 4.18. The
438 variations of PV are mostly due to variations of ζ and ϕ and less due to variations of f , which is
439 the red line sloping gently down to the right. The other two curves (blue and green) were chosen
440 to bracket the data and were used as initial conditions in a model study²¹ that is described in the
441 discussion section. The data points are given in Source Data Table SD3.

442

443 Data Availability

444 JIRAM data are available at the Planetary Data System (PDS) online ([https://pds-](https://pds-atmospheres.nmsu.edu/data_and_services/atmospheres_data/JUNO/jiram)
445 [atmospheres.nmsu.edu/data_and_services/atmospheres_data/JUNO/jiram](https://pds-atmospheres.nmsu.edu/data_and_services/atmospheres_data/JUNO/jiram)). The filenames of the
446 images are in Supplementary Table S1. Source data used in this report include calibrated,
447 geometrically controlled, radiance data mapped onto an orthographic projection centered on the
448 north pole and velocity vectors derived from the radiance data. These data products, about 150
449 MB in volume, are Source Data Tables SD1, SD2, and SD3.

450

451

452 References

- 453 1. Orton, G. S. *et al.* The first close-up images of Jupiter's polar regions: Results from the Juno
454 mission JunoCam instrument. *Geophys. Res. Lett.* **44**, 4599–4606 (2017).
- 455 2. Adriani, A. *et al.* Clusters of cyclones encircling Jupiter's poles. *Nature* **555**, 216+ (2018).

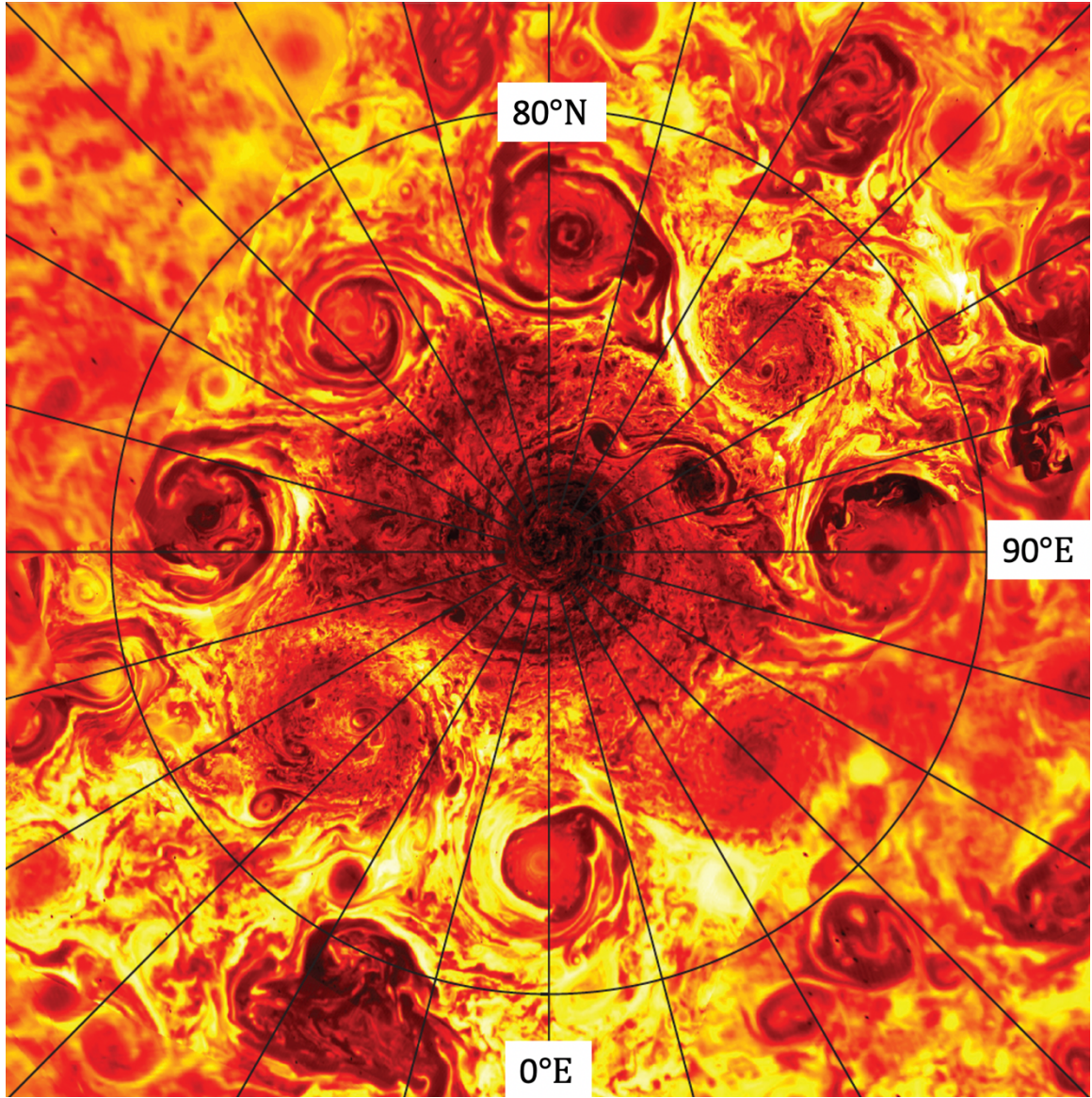
- 456 3. Tabataba-Vakili, F. *et al.* Long-term tracking of circumpolar cyclones on Jupiter from polar
457 observations with JunoCam. *Icarus* **335**, UNSP 113405 (2020).
- 458 4. Adriani, A. *et al.* Two-year observations of the Jupiter polar regions by JIRAM on board
459 Juno. *J. Geophys. Res.* (2020) doi:DOI: 10.1029/2019JE006098201.
- 460 5. Mura, A., Adriani, A. & Bracco, A. Oscillations and stability of the Jupiter polar cyclones.
461 *Nature Astronomy* (2021).
- 462 6. Grassi, D. *et al.* First estimate of wind fields in the Jupiter polar regions from JIRAM-Juno
463 images. *J. Geophys. Res.-Planets* **123**, 1511–1524 (2018).
- 464 7. Orton, G. S. & Yanamandra-Fisher, P. A. Saturn’s temperature field from high-resolution
465 middle-infrared imaging. *Science* **307**, 696–698 (2005).
- 466 8. Dyudina, U. A. *et al.* Dynamics of Saturn’s south polar vortex. *Science* **319**, 1801–1801
467 (2008).
- 468 9. Dyudina, U. A. *et al.* Saturn’s south polar vortex compared to other large vortices in the
469 Solar System. *Icarus* **202**, 240–248 (2009).
- 470 10. Sommeria, J., Meyers, S. & Swinney, H. Laboratory model of a planetary eastward jet.
471 *Nature* **337**, 58–61 (1989).
- 472 11. Allison, M., Godfrey, D. & Beebe, R. A wave-dynamic interpretation of Saturn’s polar
473 hexagon. *Science* **247**, 1061–1063 (1990).
- 474 12. Aguiar, A. C. B., Read, P. L., Wordsworth, R. D., Salter, T. & Yamazaki, Y. H. A laboratory
475 model of Saturn’s North Polar Hexagon. *Icarus* **206**, 755–763 (2010).
- 476 13. Sanchez-Lavega, A. *et al.* The long- term steady motion of Saturn’s hexagon and the stability
477 of its enclosed jet stream under seasonal changes. *Geophysical Research Letters* **41**, 1425–
478 1431 (2014).

- 479 14. Morales-Juberias, R., Sayanagi, K. M., Simon, A. A., Fletcher, L. N. & Cosentino, R. G.
480 Meandering shallow atmospheric jet as a model of Saturn's north-polar hexagon.
481 *Astrophysical Journal Letters* **806**, (2015).
- 482 15. Scott, R. K. Polar accumulation of cyclonic vorticity. *Geophys. Astrophys. Fluid Dyn.* **105**,
483 409–420 (2011).
- 484 16. O'Neill, M. E., Emanuel, K. A. & Flierl, G. R. Polar vortex formation in giant-planet
485 atmospheres due to moist convection. *Nature Geoscience* **8**, 523-U118 (2015).
- 486 17. O'Neill, M. E., Emanuel, K. A. & Flierl, G. R. Weak jets and strong cyclones: Shallow-water
487 modeling of giant planet polar caps. *J. Atmos. Sci.* **73**, 1841–1855 (2016).
- 488 18. Brueshaber, S. R., Sayanagi, K. M. & Dowling, T. E. Dynamical regimes of giant planet
489 polar vortices. *Icarus* **323**, 46–61 (2019).
- 490 19. Siegelman, L., Young, W. R., & Ingersoll, A. P. (2022). Polar vortex crystals: Emergence
491 and structure. *Proceedings of the National Academy of Sciences of the United States of*
492 *America*, *119*(17), e2120486119. <https://doi.org/10.1073/pnas.2120486119>
- 493 20. Siegelman, L., Klein, P., Ingersoll, A. P., Ewald, S. P., Young, W. R., Bracco, A., et al.
494 (2022). Moist convection drives an upscale energy transfer at Jovian high latitudes. *Nature*
495 *Physics*, *18*(3), 357–+. <https://doi.org/10.1038/s41567-021-01458-y>
- 496 21. Li, C., Ingersoll, A. P., Klipfel, A. P. & Brettle, H. Modeling the stability of polygonal
497 patterns of vortices at the poles of Jupiter as revealed by the Juno spacecraft. *Proc. Natl.*
498 *Acad. Sci. U. S. A.* **117**, 24082–24087 (2020).
- 499 22. Thomson, S. I. & McIntyre, M. E. Jupiter's unearthly jets: A new turbulent model exhibiting
500 statistical steadiness without large-scale dissipation*. *J. Atmos. Sci.* **73**, 1119–1141 (2016).

- 501 23. Rubio, A. M., Julien, K., Knobloch, E. & Weiss, J. B. Upscale energy transfer in three-
502 dimensional rapidly rotating turbulent convection. *Phys. Rev. Lett.* **112**, 144501 (2014).
- 503 24. Novi, L., von Hardenberg, J., Hughes, D. W., Provenzale, A. & Spiegel, E. A. Rapidly
504 rotating Rayleigh-Benard convection with a tilted axis. *Phys. Rev. E* **99**, 053116 (2019).
- 505 25. Yadav, R. K., Heimpel, M. & Bloxham, J. Deep convection-driven vortex formation on
506 Jupiter and Saturn. *Sci. Adv.* **6**, eabb9298 (2020).
- 507 26. Kopyla, P. J., Mantere, M. J. & Hackman, T. Starspots due to large-scale vortices in rotating
508 turbulent convection. *Astrophys. J.* **742**, 34 (2011).
- 509 27. Heimpel, M., Gastine, T. & Wicht, J. Simulation of deep-seated zonal jets and shallow
510 vortices in gas giant atmospheres. *Nature Geoscience* **9**, 19+ (2016).
- 511 28. Cai, T., Chan, K. L. & Mayr, H. G. Deep closely packed long-lived cyclones on Jupiter's
512 poles. *The Planetary Science Journal* **2:81**, 19 (2021).
- 513 29. Ingersoll, A. & Cuzzi, J. Dynamics of Jupiter's cloud bands. *J. Atmos. Sci.* **26**, 981+ (1969).
- 514 30. Limaye, S. Jupiter - New estimates of the mean zonal flow at the cloud level. *Icarus* **65**, 335–
515 352 (1986).
- 516 31. Li, L. M. *et al.* Life cycles of spots on Jupiter from Cassini images. *Icarus* **172**, 9–23 (2004).
- 517 32. Garcia-Melendo, E., Perez-Hoyos, S., Sanchez-Lavega, A. & Hueso, R. Saturn's zonal wind
518 profile in 2004-2009 from Cassini ISS images and its long-term variability. *Icarus* **215**, 62–
519 74 (2011).
- 520 33. Dowling, T. A relationship between potential vorticity and zonal wind on Jupiter. *J. Atmos.*
521 *Sci.* **50**, 14–22 (1993).
- 522 34. Achterberg, R. & Ingersoll, A. A normal-mode approach to Jovian atmospheric dynamics. *J.*
523 *Atmos. Sci.* **46**, 2448–2462 (1989).

- 524 35. Wong, M. H., de Pater, I., Asay-Davis, X., Marcus, P. S. & Go, C. Y. Vertical structure of
525 Jupiter's Oval BA before and after it reddened: What changed? *Icarus* **215**, 211–225 (2011).
- 526 36. Hammel, H. *et al.* HST Imaging of atmospheric phenomena created by the impact of Comet
527 Shoemaker-Levy-9. *Science* **267**, 1288–1296 (1995).
- 528 37. Rhines, P. Waves and turbulence on a beta-plane. *J. Fluid Mech.* **69**, 417–443 (1975).
- 529 38. Theiss, J. Equatorward energy cascade, critical latitude, and the predominance of cyclonic
530 vortices in geostrophic turbulence. *Journal of Physical Oceanography* **34**, 1663–1678
531 (2004).
- 532 39. Scott, R. K. & Polvani, L. M. Forced-dissipative shallow-water turbulence on the sphere and
533 the atmospheric circulation of the giant planets. *J. Atmos. Sci.* **64**, 3158–3176 (2007).
- 534 40. Mied, R. & Lindemann, G. Propagation and evolution of cyclonic Gulf-Stream rings. *J.*
535 *Phys. Oceanogr.* **9**, 1183–1206 (1979).
- 536 41. Chassignet, E. & Cushman-Roisin, B. On the influence of a lower layer on the propagation
537 of nonlinear oceanic eddies. *J. Phys. Oceanogr.* **21**, 939–957 (1991).
- 538 42. Adriani, A. *et al.* JIRAM, the Jovian Infrared Auroral Mapper. *Space Sci. Rev.* **213**, 393–446
539 (2017).
- 540 43. Gonzalez, R. C. & Woods, R. E. *Digital Image Processing*. (Pearson, 2016).
- 541 44. Garcia-Ortega, E., Lopez, L. & Sanchez, J. L. Diagnosis and sensitivity study of two severe
542 storm events in the Southeastern Andes. *Atmos. Res.* **93**, 161–178 (2009).
- 543 45. Marion, G. R. & Trapp, R. J. The dynamical coupling of convective updrafts, downdrafts,
544 and cold pools in simulated supercell thunderstorms. *J. Geophys. Res.-Atmos.* **124**, 664–683
545 (2019).

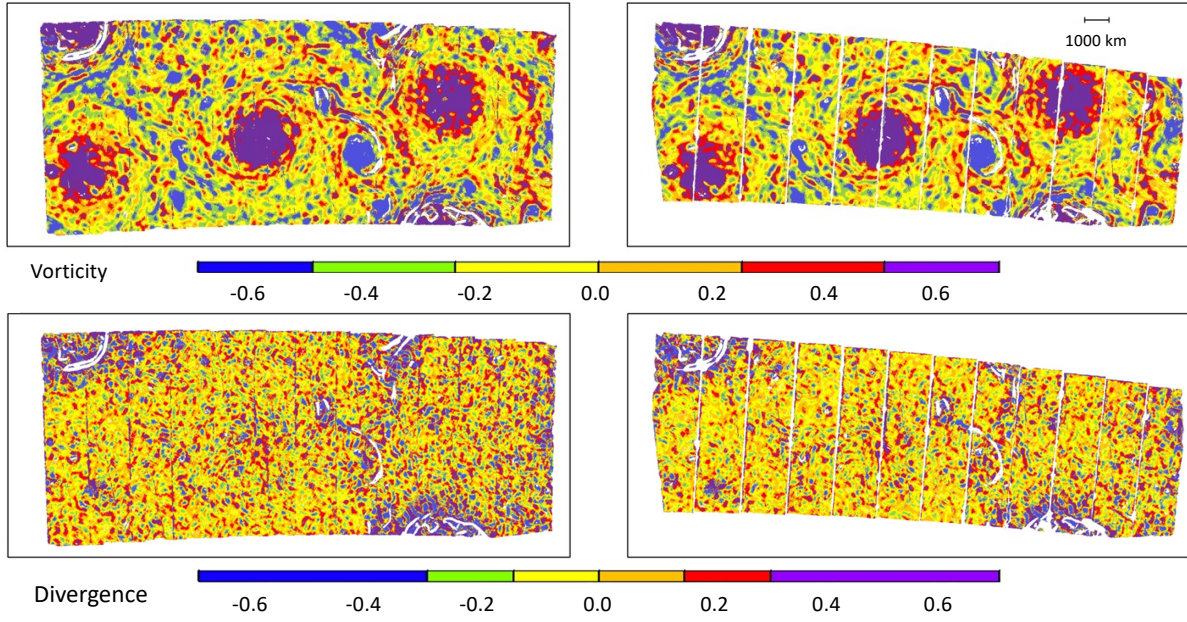
- 546 46. Solov'ev, A. A., Parfinenko, L. D., Efremov, V. I., Kirichek, E. A. & Korolkova, O. A.
547 Structure of photosphere under high resolution: granules, faculae, micropores, intergranular
548 lanes. *Astrophys Space Sci* **364**, 222 (2019).
- 549 47. Jukes, M. Quasi-geostrophic dynamics of the tropopause. *J. Atmos. Sci.* **51**, 2756–2768
550 (1994).
- 551 48. Held, I. M., Pierrehumbert, R. T., Garner, S. T. & Swanson, A. Surface quasi-geostrophic
552 dynamics. *J. Fluid Mech.* **282**, 1–20 (1995).
- 553 49. Lapeyre, G., & Klein, P. (2006). Dynamics of the upper oceanic layers in terms of surface
554 quasigeostrophy theory. *Journal of Physical Oceanography*, *36*(2), 165–176.
555 <https://doi.org/10.1175/JPO2840.1>
- 556 50. Lapeyre, Guillaume. (2017). Surface Quasi-Geostrophy. *Fluids*, *2*(1), 7-28.
557 <https://doi.org/10.3390/fluids2010007>
- 558 51. Young, R. M. B., & Read, P. L. (2017). Forward and inverse kinetic energy cascades in
559 Jupiter's turbulent weather layer. *Nature Physics*, *13*, 1135-1140.
560 <https://doi.org/10.1038/nphys4227>
- 561 52. Scarica, P., Grassi, D., Mura, A., Adriani, A., Ingersoll, A., Li, Cheng, & 13 more. (2022).
562 Stability of the Jupiter southern polar vortices inspected through vorticity. *Geophys. Res.*
563 *Lett.* Submitted.
- 564



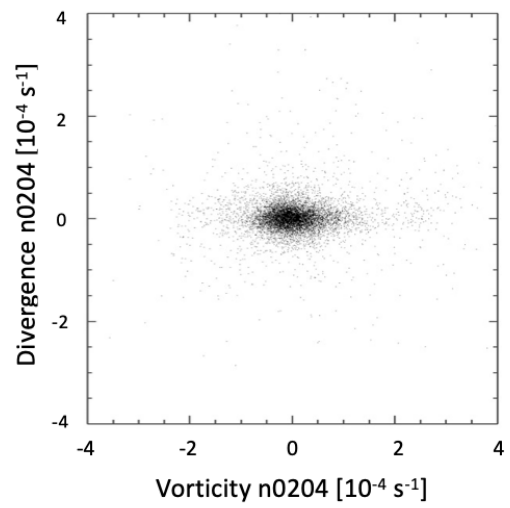
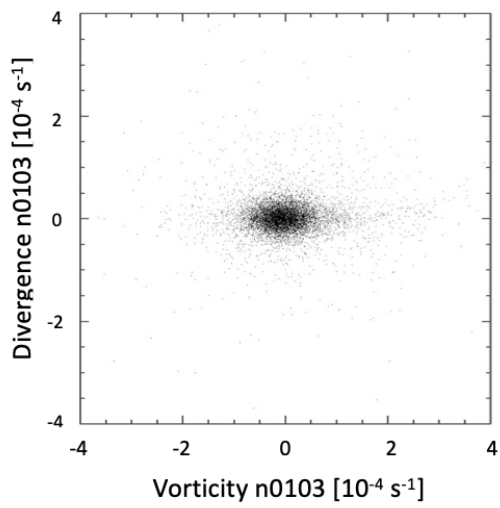
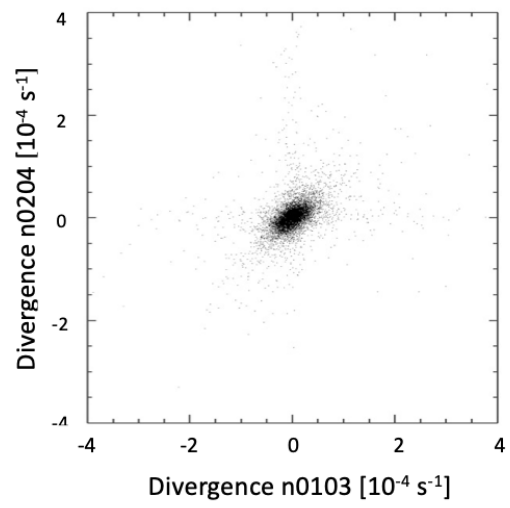
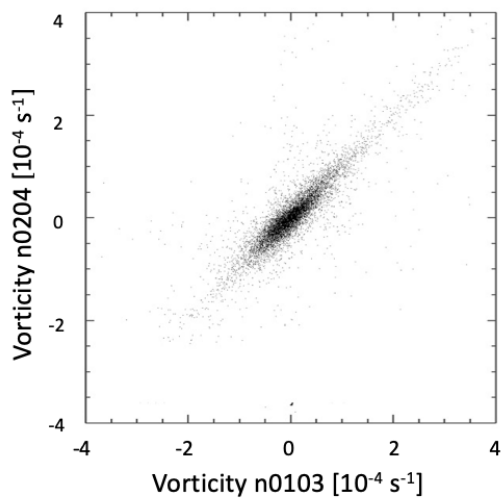
565

566 Figure 1

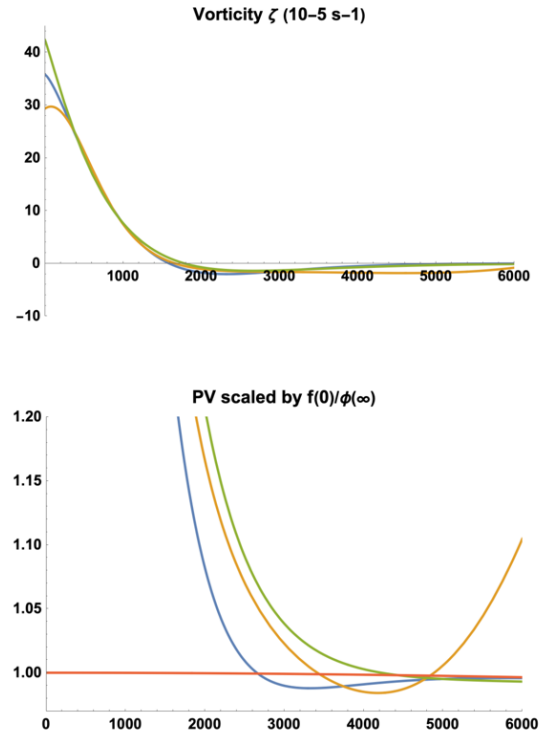
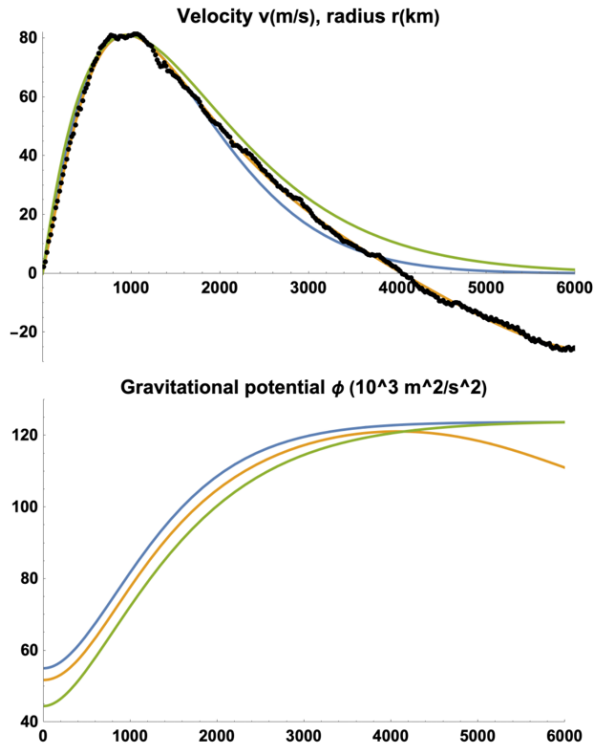
567



568
 569 Figure 2
 570



571
572 Figure 3
573



574
575 Figure 4